Fast-Ignition Target Design and Experimental-Concept Validation on OMEGA

Introduction

The fast-ignitor concept for inertial confinement fusion[1,2] has shown significant promise due to successful small-scale integrated experiments.[3,4] It makes it possible to use lower driver energies than conventional hot-spot ignition[5] and has the potential for higher gains. The fast-ignitor concept separates the fuel assembly and fuel heating by using an ultrafast laser in addition to a driver that compresses the fuel to high density. The ultrafast laser produces relativistic electrons with high efficiency (up to 50% has been reported[6]) that heat the fuel. Options for the compression driver are laser or heavy-ion-beam–heated hohlraums or laser direct drive.[7]

Many challenges remain for the fast-ignitor concept. The first is to demonstrate the required compression of the fuel to areal densities required for ignition. The conversion efficiency from ultrafast laser to energetic electrons must be high at ignition-relevant intensities, energies, and pulse lengths. The energy distribution of the hot electrons must be compatible with the areal density of the compressed core to ensure that the electrons deposit most of their energy into a hot spot of at least 0.3 g/cc cm (Ref. 8). Another challenge is the transport of relativistic electrons from the critical-density region ($n_e \sim 10^{21}$ cm^{-3} for a typical 1-μm laser), where the ultrafast laser is absorbed and converted into electrons, to the compressed fuel—a distance that can be hundreds of microns in an ignition-scale target. For an electron-beam divergence of ~20°, the overlap between the electron beam originating from a small focal spot (~10-μm radius) and the dense core with a diameter of <50 μm would be very small.[9,10] Two solutions have been proposed to minimize this standoff distance: a channeling beam to bore a hole in the plasma atmosphere around the core,[2,11] which would allow the ultrafast laser to be absorbed closer to the core, and a re-entrant cone to keep the path of the ultrafast laser free of plasma and bring it as close as possible to the dense core.[3,12] The cone-in-shell concept, while advantageous with respect to the electron transport, breaks the symmetry of the spherical fuel assembly, which could limit the fuel areal density that can be achieved with a given driver energy. Another issue for cone-in-shell targets is plasma filling the inside of the cone from the shock wave that the high-pressure core plasma sends through the gold cone. Self-generated electromagnetic fields from the propagation of the electron beam in plasma will modify both the transport and the energy-deposition characteristics. The transport and energy deposition of the fusion alpha particles in near-ignition plasma conditions could significantly change the plasma conditions in the assembled fuel.

All of these physics areas will be experimentally accessible with the combined OMEGA/OMEGA EP Facility at LLE. OMEGA EP[13] provides two short-pulse (~1 ps to 100 ps), high-energy laser beams with an energy of up to 2.6 kJ per beam at 1.053 μm, integrated into the existing OMEGA[14] Laser Facility (60 beam, 30 kJ at 0.35 μm). The OMEGA EP beams can be combined collinearly and coaxially and routed to either the existing OMEGA target chamber or the new OMEGA EP target chamber. The combined beams allow the channeling approach to fast ignition (FI) to be studied under realistic conditions for the first time, whereas only one beam is required for cone-in-shell experiments. The OMEGA/OMEGA EP Facility will be best suited to perform integrated fast-ignition experiments because of OMEGA's unique ability to compress cryogenic D_2 and DT targets.[15,16] To study alpha transport under realistic conditions, the areal density of the compressed core must be of the order of the hot-spot areal density of an ignition target, ~0.3 g/cm^2 (Ref. 8), which could be achieved in high-performance cryogenic-DT implosions on OMEGA.[17]

This article describes several important components of LLE's comprehensive scientific program to investigate the physics of the fast-ignitor concept. The following sections (1) introduce the OMEGA/OMEGA EP integrated laser facility; (2) describe hydrodynamic experiments on high-areal-density implosion and fuel assembly with cone-in-shell targets; (3) discuss experiments that measure the conversion efficiency from laser light into energetic electrons and the development of a coherent transition radiation diagnostic to investigate the hot-electron transport; (4) summarize simulations of integrated fast-ignitor physics experiments on OMEGA EP and full-scale, high-gain, fast-ignition experiments; and (5) provide a short summary of the information presented.

Laser System

The OMEGA EP Laser Facility is housed in a structure on the south side of the existing OMEGA laser building (see Fig. 115.11). The OMEGA EP target chamber is due east of the existing OMEGA target chamber. The OMEGA Laser System delivers up to 30 kJ of UV light in 60 beams arrayed in a "soccer ball" symmetry for uniform illumination of spherical implosion targets.[14] OMEGA has an elaborate pulse-shaping system, which can provide up to ~4-ns-long, highly shaped pulses with a contrast of up to 100. The individual OMEGA beams are smoothed by distributed phase plates (DPP's),[18] two-dimensional smoothing by spectral dispersion[19] with 1-THz bandwidth in the UV, and polarization smoothing.[20]

The four new OMEGA EP beamlines are located to the south of the compression chamber and the new target chamber. The beamlines use a folded beam path similar to the architecture[21] of the National Ignition Facility (NIF)—an upper level that includes a 7-disk booster amplifier and a transport spatial filter, and a lower level that includes an 11-disk main amplifier, a cavity spatial filter, a plasma-electrode Pockels cell (PEPC),[22] and a deformable mirror. A second polarizer is inserted between the PEPC and the cavity spatial filter to protect the laser system against IR light reflected from the target when the beamline is operated in short-pulse mode. Two of the beams can be compressed using four 141-cm × 41-cm diffraction-grating units, with each unit consisting of three multilayer-dielectric–grating tiles.[23,24] A deformable mirror placed after the last grating unit provides further wavefront correction in each beamline. The beams are either combined before leaving the compression chamber and propagate coaxially through evacuated tubes to the OMEGA or OMEGA EP target chamber, or they can be directed into the OMEGA EP chamber on separate paths in an orthogonal configuration. An *f*/2 off-axis parabola focuses the short-pulse beam to provide a small focal spot even with the expected phase-front distortions in such a large-scale, high-energy laser system. The beams are synchronized to each other and to the OMEGA laser pulse to better than 10-ps rms. A comprehensive set of laser diagnostics measures the laser energy, pulse duration, and, for the first time on a high-energy petawatt system, the focal-spot intensity distribution at full energy. All four beams can be used as long-pulse beams and converted into the third harmonic at 351 nm (<10 ns, up to 6.5 kJ). These beams propagate only to the OMEGA EP target chamber. The long-pulse beams are focused with *f*/6.5 lenses onto the target and are arrayed in a square with a 23° angle to their common centerline. DPP's for beam shaping will be available in 2009.

Fuel-Assembly Experiments

High fuel compression and high areal densities have been achieved on OMEGA, both with cryogenic targets[25] and room-temperature targets,[26] using highly shaped pulses that put the target on a low adiabat (ratio of the shell pressure to the Fermi-degenerate pressure). It has been shown that the areal density ρR depends primarily on the adiabat α of the target and the laser energy E:[27]

$$(\rho R)_{\max} = 2.6 \Big/ \alpha^{0.54} E_{\mathrm{MJ}}^{0.33}. \qquad (1)$$

The cryogenic targets are 10-μm-thick, ~430-μm-outer-radius CD shells, filled with D_2 to form a 95-μm-thick layer at the inside of the CD shell at cryogenic temperatures.

The pulse shape for the cryogenic target (Fig. 115.12) uses a decaying-shock-adiabat shaping picket[28] and a slowly rising

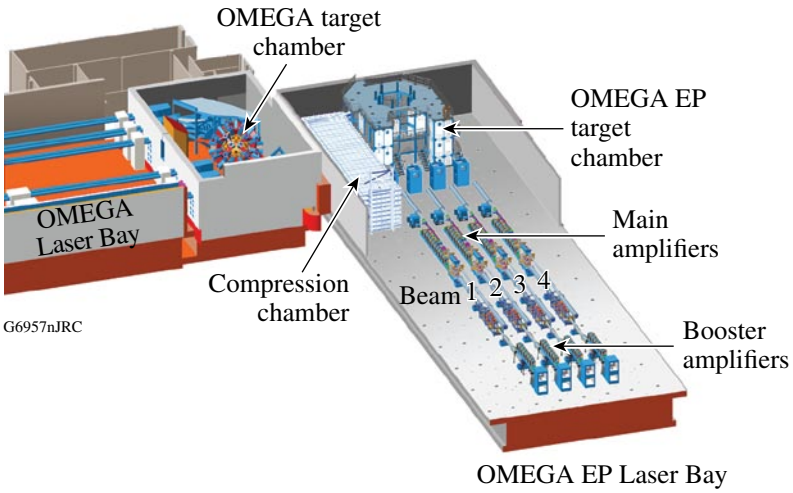

Figure 115.11
Schematic of the expanded OMEGA Laser Facility. The new OMEGA EP laser adjacent to the existing 60-beam OMEGA facility includes four NIF-like beamlines, a compression chamber, and a new target chamber. Two of the four beams can be run in short-pulse mode and can be directed into either target chamber. All four beams can be converted into UV and used in the OMEGA EP target chamber.

main pulse to put the cryogenic D_2 fuel on an adiabat of $\alpha \sim 2$. The areal density of the imploded targets is inferred from the energy downshift in the secondary proton spectrum.[29] These protons are created by D^3He fusion reactions, which are secondary reactions in D_2 fuel. Figure 115.13 shows a measured secondary proton spectrum from the cryogenic target compared to 1-D *LILAC*[30] simulations.[25] An areal density of ~200 mg/cm^2 can be inferred from the spectrum, which is more than 80% of the clean 1-D predictions. The density of the compressed D_2 approaches ~100 g/cm^3—a 500-fold compression of the original D_2-ice density. In the room-temperature experiments, 40-μm-thick, 430-μm-outer-radius plastic shells coated outside with a 0.1-μm layer of aluminum and filled with D_2 gas with pressure ranging from 8 to 25 atm were imploded using relaxation adiabat-shaping, ~16- to 20-kJ UV laser pulses.[26,31,32] A typical experimental pulse shape that puts the room-temperature plastic targets on an adiabat of $\alpha \sim 1.5$ is shown in Fig. 115.12. A picket at the beginning of the pulse and a spike at the end of the pulse were used to optimize the implosion for high yield and high areal density. The room-temperature targets also showed areal densities of up to ~200 mg/cm^2 and densities of the order of 100 g/cm^3, which translates into a 100-fold compression.

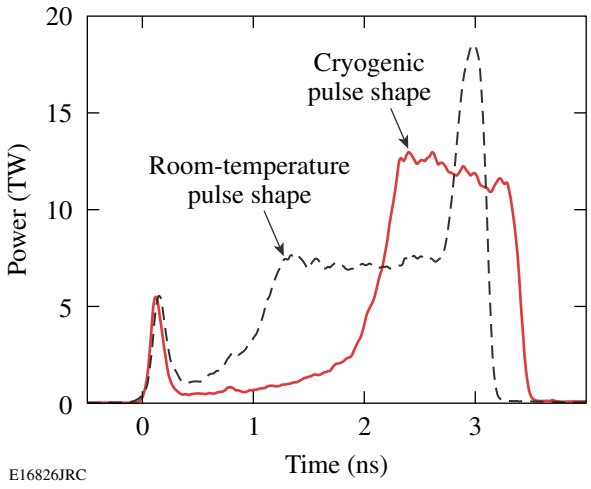

Figure 115.12
Laser pulse shapes used in the low-adiabat OMEGA cyrogenic (solid) and room-temperature (dashed) target implosions.

Fuel assembly in direct-drive cone-in-shell targets has been investigated using experiments on OMEGA in both indirect-[33] and direct-drive[34] geometries, including the achievable areal densities and filling the cone with plasma. Gas-tight targets were developed for the direct-drive experiments to be able to fill the targets with D_2 or D^3He, which makes it possible to use nuclear diagnostics to measure the areal density achieved in the implosion. The targets were 24- to 40-μm-thick CH shells of ~870-μm outer diameter, with a hollow gold cone with an opening angle of 70° or 35° inserted through a hole in the shell (Fig. 115.14).[34] A step on the cone defines the distance between the cone tip and the center of the shell, typically 30±10 μm. The cone has a thickness of ~100 μm outside the shell and 10 μm inside the shell and ends in a 30-μm-thick hyperbolic-shaped tip. For some experiments the cone tip was

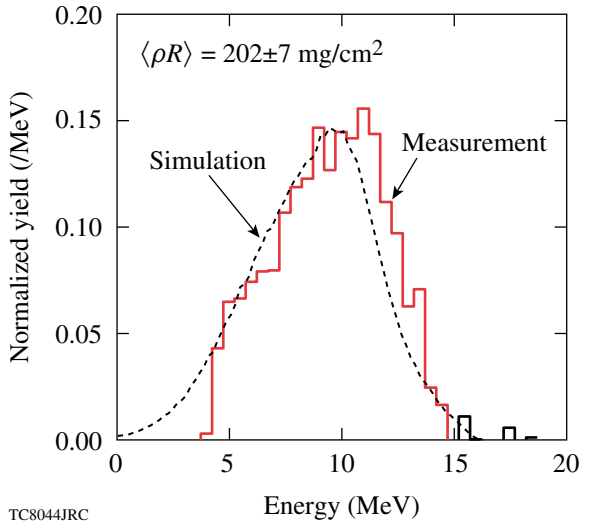

Figure 115.13
Measured secondary-proton spectrum (solid line) for the cryogenic target. The dashed line shows the calculated spectrum from the 1-D hydrocode.

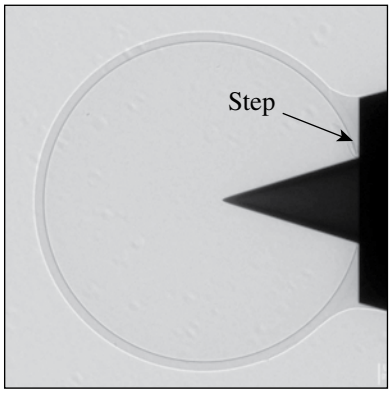

Figure 115.14
Radiograph of a gas-tight, fast-ignitor cone-in-shell target. A gold cone with an opening angle of 35° is inserted through a hole in a 24-μm-thick CH shell of ~870-μm outer diameter. A step on the cone defines the location of the cone tip at a distance of 30±10 μm to the center of the shell. It also provides a convenient interface to apply enough glue to make the assembly gas tight.

cut off to form a 15-μm-thick flat tip. Most experiments used 54 of the 60 OMEGA beams, at 351-nm wavelength, with a 1-ns square pulse and ~21 kJ of total energy or a highly shaped pulse of ~3-ns duration and ~20-kJ energy. For some experiments, 15 beams with a total energy of ~6 kJ were diverted to a backlighter foil and focused to a spot size of 600 μm. The target was irradiated using 35 of the remaining beams with ~11 kJ of laser energy.

X-ray framing cameras[35] were used to acquire backlit images of the fuel assembly around the cone tip. Figure 115.15 shows a backlit image of a cone-in-shell target (lower half) irradiated with a 1-ns square pulse at peak density compared to a 2-D *DRACO*[36] hydrodynamic simulation (upper half). The image shows a dense core ~100 μm from the cone tip, with lower-density plasma in between. An areal density of ~70 mg/cm^2 was measured for a 35° cone target using nuclear diagnostics—more than 60% of what a 1-D simulation predicts for an equivalent full sphere.[34] Mixing does not seem to be an issue in these direct-drive cone experiments,[34] and the hydro-efficiency penalty from the cone is not very big. A streaked optical pyrometer (SOP)[37] was used to investigate the filling of the inside of the cone. The high-pressure core plasma sends a shock wave through the gold cone that creates a plasma inside the cone when it breaks out. This could significantly increase the electron propagation distance. SOP uses an optical system that images the inside of the tip of the cone onto the slit of the streak camera with an ~10-μm spatial resolution and a 500-μm field of view. The breakout of the shock driven by the pressure from the core produces a short burst of light.

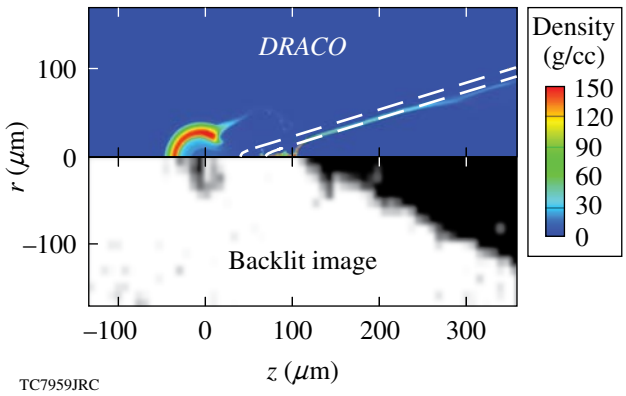

Figure 115.15
Backlit framing-camera image from a target filled with 10 atm of D_2 and imploded using a 1-ns square pulse at 11-kJ laser energy, compared to a 2-D *DRACO* radiation hydrodynamic code simulation.

Figure 115.16 shows a lineout through the center of the SOP trace from a 35° cone target with a 15-μm-thick flat tip irradiated by a highly shaped pulse at 20-kJ energy, as well as the areal density of the compressed core as predicted by the 2-D hydrocode *DRACO* and the drive-laser pulse shape. The shock signal starts just after the time of peak compression as calculated by *DRACO*. The absolute timing uncertainty of SOP is estimated to be ~100 ps. This shows that with the current designs the inside of the cone is free of plasma at the time when the short-pulse laser would propagate. Since the projected range for a 1-MeV electron in gold is of the order of ~50 μm (Ref. 38), the gold tip must be as thin as possible to avoid excessive energy loss of the fast electrons. In an optimized cryogenic capsule, the core would produce a lower pressure on the cone due to the lower average ionization of hydrogenic plasma compared to CH plasma.

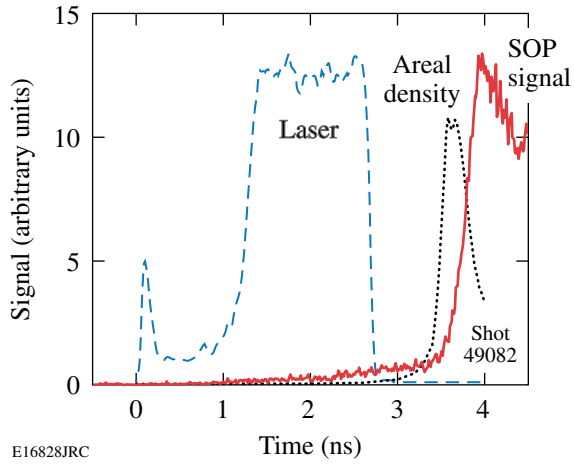

Figure 115.16
Lineout through the center of the SOP signal (solid line) of a cone-in-shell target with a 35° opening angle irradiated by a shaped pulse at 20 kJ. The dashed line shows the laser pulse power, and the dotted line represents the calculated evolution of the areal density.

Short-Pulse Experiments and Diagnostics

The conversion efficiency from laser energy into energetic electrons $\eta_{L\to e}$ has been measured using K-shell spectroscopy of reduced-mass Cu targets.[39] It has been shown that the normalized fast-electron–induced K_α yield from reduced-mass targets is approximately constant above 10^{18} W/cm^2 and can be readily used to infer $\eta_{L\to e}$ (Refs. 40 and 41). The heating of these reduced-mass targets is sufficient to affect the inner-shell fluorescence probabilities.[41] Ionization of the outer shells of copper at high temperature affects the M ⟶ K and the L ⟶ K transition probabilities and causes a deviation in the ratio of the emitted

number of K_β and K_α photons. This is used to infer the electron temperature of the target and allows the conversion efficiency $\eta_{L\to e}$ to be inferred independently from the absolute K_α yield by using a model for the equation of state of copper.[41]

The experiments have been performed on both the Rutherford Appleton Laboratory PW facility[42] and the Multi-Terawatt (MTW) laser at LLE.[43] The Vulcan PW laser delivers up to 500 J of energy with a pulse duration as short as 0.5 ps at a wavelength of 1.054 μm, focused by an *f*/3 off-axis parabola onto the target. Roughly 30% of the laser energy is contained in a 7-μm full width at half maximum (FWHM) spot. The MTW laser delivered 1- to 5-J, 1-ps pulses at a wavelength of 1.053 μm and was focused by an *f*/2 off-axis parabola at normal incidence to the target. The focal spot has an FWHM between 4 to 6 μm containing ~50% of the laser energy, with a peak intensity of 2×10^{19} W/cm^2.

Copper foils ranging between $20\times20\times2$ μm^3 and $500\times500\times50$ μm^3 were used as targets. They were mounted by using either a 17-μm-diam silicon carbide stalk or, in the case of the smallest targets, a pair of 1-μm-diam spider silk threads.

The K-shell line radiation was measured using a single-photon–counting spectrometer[44] based on an SI 800-145 x-ray back-illuminated, charge-coupled device (CCD).[45] Various copper filters between 75 to 150 μm were used to optimize the signal-to-background ratio of the K-shell emission. Figure 115.17(a) (Ref. 39) shows the measured conversion efficiency of laser energy into K_α photons emitted from $500\times500\times20$-μm^3 copper targets as a function of the laser intensity. The K_α photon yield increases up to intensities of 10^{18} W/cm^2 and stays constant at higher intensity. The data from Fig. 115.17 are compared to a model of K_α photon production, which assumes an exponentially distributed fast-electron spectrum $f(E)=\exp\left(-E/T_e\right)$, where T_e is calculated from the laser intensity through the ponderomotive scaling.[46]

$$T_e\,[\mathrm{MeV}] = 0.511\left[\left(1+I_{18}\lambda_{\mu m}^2/1.37\right)^{0.5}-1\right], \qquad (2)$$

where E is the electron energy, T_e is the electron temperature, I_{18} is the laser intensity in units of 10^{18} W/cm^2, and $\lambda_{\mu m}$ is the laser wavelength in microns. The energy loss of the fast electrons is calculated using the continuous slowing down for cold approximation solid-density copper.

The model assumes that all electrons are reflected at the target boundaries from electrostatic sheath fields[47,48] and deposit all their energy in the target (refluxing). Relativistic corrections to the copper K-shell ionization cross section[49] are included, and the only free parameter in the model is the conversion efficiency $\eta_{L\to e}$. A laser-to-electron energy-conversion efficiency $\eta_{L\to e}$ = (20±10)% can be inferred by comparing the experimental data with the predictions of this model. The discrepancies in the observed K_α yield at lower laser intensities are most likely due to the assumption of ponderomotive scaling, which breaks down at a laser irradiance below 10^{18} W/cm^2 μm^2 (Ref. 46).

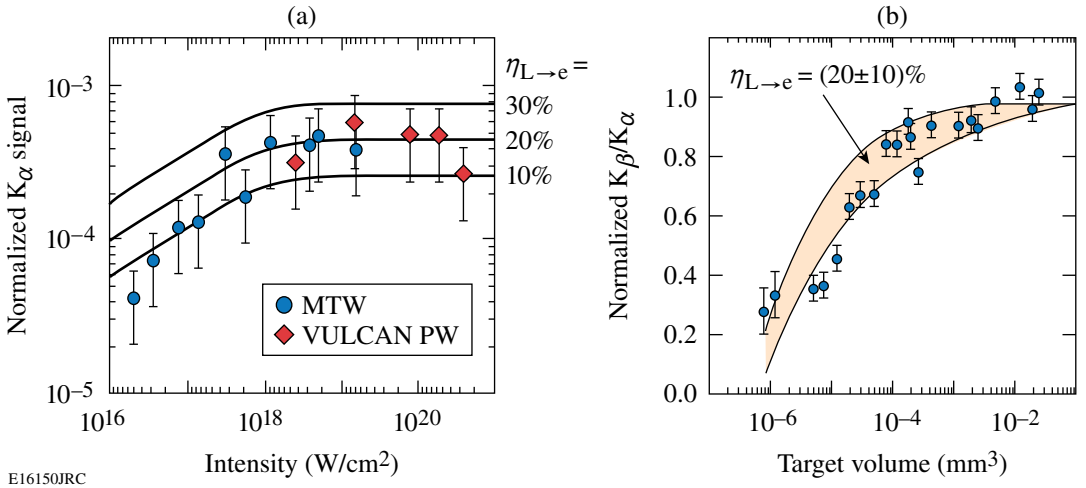

Figure 115.17
(a) Energy in K_α photons (normalized to the laser energy) emitted by a $500\times500\times20$-μm^3 copper target as a function of laser intensity. The curves correspond to the total calculated K_α yield at a given laser-to-electron-energy-conversion efficiency $\eta_{L\to e}$. (b) Ratio of the number of K_β to K_α photons (normalized to the cold material value) as a function of target volume. Numerical calculations of K_β/K_α are shown as a function of target volume caused by target heating, assuming $\eta_{L\to e}$ = (20±10)%.

Figure 115.17(b) (Ref. 39) shows the measurement of the change in the ratio of the number of emitted K_β and K_α photons $\left(K_\beta/K_\alpha\right)$ normalized to the cold material value as a function of the target volume at a constant laser intensity of 2×10^{19} W/cm^2. Numerical target-heating calculations using the implicit-hybrid particle-in-cell code *LSP*[50] infer the energy content of the fast electrons from the reduction in the ratio of K_β/K_α (Ref. 41). The collisional-radiative code *PrismSPECT*[51] was used to determine the target's ion-population distribution. Assuming a conversion efficiency of $\eta_{L\to e} = (20\pm10)\%$, the calculation reproduces the observed variation in the ratio $\left(K_\beta/K_\alpha\right)$ with target volume, which is consistent with the efficiencies inferred from the absolute K_α yield. This technique can be readily extended to laser energies on the multikilojoule level and pulse durations >10 ps on OMEGA EP, much closer to the fast-ignitor laser conditions as in the present small-scale experiments.

A promising technique that provides information about the transport of the energetic electrons generated in the short-pulse laser–plasma interaction is the measurement of transition radiation (TR).[52] TR is emitted when a charged particle passes through a refractive-index interface[53]—in this case, energetic electrons exiting the target into vacuum. The emitted electromagnetic energy is very small for a single electron. However, the laser-generated energetic-electron distribution typically has a highly correlated longitudinal electron-density structure, which leads to a considerable coherent enhancement, producing coherent transition radiation (CTR).[54] The two dominant electron-acceleration processes produce structures at different frequencies: resonance absorption[55] accelerates electrons into the target once every optical cycle, whereas the $\vec{v}\times\vec{B}$ force[46] accelerates electrons twice every optical cycle, generating a CTR signal at the first or second harmonic of the laser frequency, respectively. The spatial-intensity distribution and spectrum of the CTR emission measured at the backside of the target provide information about the electron transport, especially the spatial distribution and divergence of the coherent part of the electron distribution exiting the target and the slope or temperature of the longitudinal energy distribution.

A transition radiation diagnostic (TRD)[56] has been developed to acquire high-resolution images of the target's rear-side optical emission at the second harmonic ($\lambda \sim 527$ nm) for experiments conducted on the MTW laser. The optical design is shown in Fig. 115.18(a) (Ref. 56). A commercial 20× infinity corrected objective[57] collects the optical emission from the target's rear

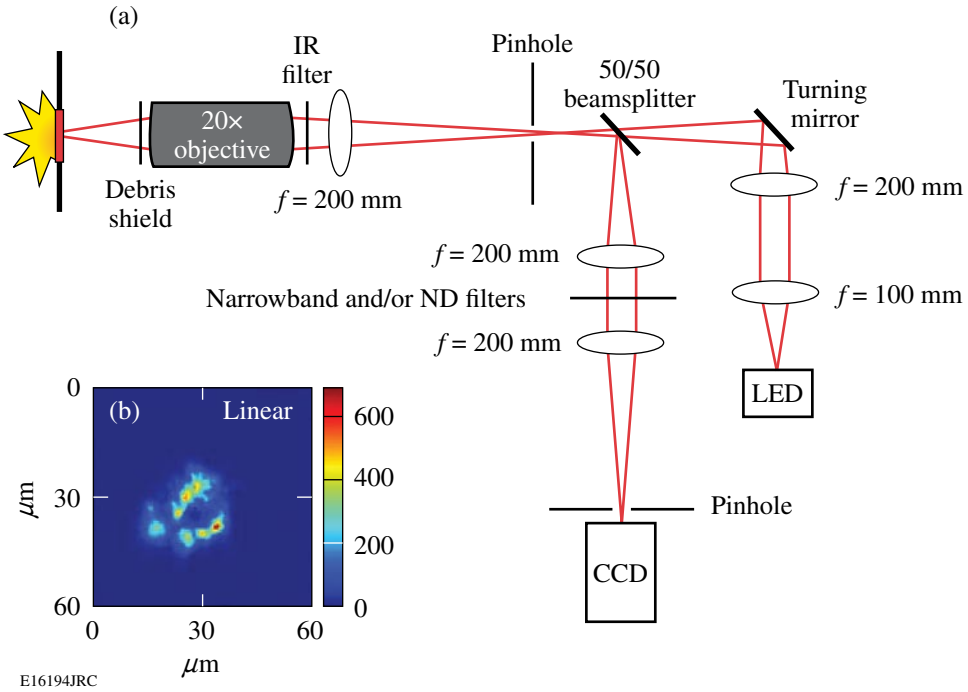

Figure 115.18
(a) Optical design of the transition radiation detector. A high-quality microscope objective and an optical system of three lenses image the rear surface of the target onto a CCD detector. Filters and pinholes are used to minimize background contributions. The right arm of the system is used for pre-shot focusing. (b) Image of the rear-side optical CTR emission from a 20-μm-thick aluminum foil. The scale is logarithmic and the intensity is expressed in arbitrary units. A number of ~2-μm-diam filaments are contained within a 15-μm-diam emission region.

surface. A sacrificial 150-μm-thick glass microscope cover protects the objective from target debris. The objective is mounted on a high-resolution (20-nm step), motorized, 1-D linear actuator. Filters prevent 1ω laser light from propagating and narrow the spectral acceptance of the optical system to a 24-nm band centered on λ = 529 nm. An optical system of three 200-mm-focal-length achromatic lenses and a 50/50 beam splitter transports the light to a CCD camera. This Spectral Instruments (SI) 800-series CCD uses a front-illuminated chip with 1024 × 1024, 13.5-μm × 13.5-μm pixels, thermo-electrically cooled to –40°C to minimize the dark current.[45] To obtain consistent high-resolution images of the target's rear-surface emission, the microscope objective must be positioned with ~1-μm precision relative to the rear surface of the target since its depth of focus is only 1.6 μm. The second arm of the optical system sends light from an ultrabright green LED (light-emitting diode) through the beam splitter and collection optics onto the target. The light reflected off small-scale surface features on the rear surface of the target is imaged onto the CCD camera. These features are used to obtain the best focus position for the objective. Extensive tests have shown that the optical resolution of the TRD in the optimum focus position is limited only by the CCD pixel size to ~1.4 μm over the full field of view.[56] The pinholes shown in Fig. 115.18(a) minimize the propagation of stray light through the system. The background from hard x rays is minimized by folding the optical system through 90° so that the detector can be shielded behind a 10-cm-thick lead brick wall. An additional 2-mm-thick lead shield is placed around the CCD camera to minimize single hits by scattered x rays arriving from the rear and top sides. This shielding reduces the background by more than an order of magnitude on the CCD detector.

The TRD has been used in several experiments to diagnose electron transport in solid materials. Figure 115.18(b) shows a coherent transition radiation image from the rear side of a 30-μm aluminum foil. A 5-J, 500-fs pulse from the MTW laser was focused to an ~4-μm-radius spot on the target, corresponding to a laser intensity of ~10^{19} W/cm^2. The diameter of the rear-side coherent optical emission is less than 20 μm. Structures, indicative of electron-beam filaments, superimposed on a ring-like feature are clearly visible in this region with a spatial full width at half maximum of ~2 μm. These structures are indicative of electron-beam filamentation.[58]

This instrument will be used extensively on the MTW to study the divergence and potential breakup of the electron flow through the target and to infer the slope temperature of the longitudinal electron temperature.[54] Based on the experience with this TRD on the MTW, a detector suitable for OMEGA EP is being designed.

Simulations

To understand the interaction of the electron beam with the target and its effect on the neutron production in both integrated FI experiments on OMEGA EP and high-gain FI targets, the 2-D axisymmetric radiation hydrocode *DRACO* was coupled with the 2-D/3-D hybrid particle-in-cell code *LSP*.[50] *DRACO* simulates the target implosion and the hydrodynamic reaction of the target to the fast-electron heating, using a realistic tabular equation of state, radiation transport, and α-particle transport in DT targets. *LSP* is used to simulate hot-electron transport including self-generated electromagnetic fields. The laser–plasma interaction that creates the energetic electrons is not modeled in *LSP*; a hot-electron distribution is created by promoting background electrons to higher energy according to a theoretical prescription such as Wilks's scaling law[46] and a constant conversion efficiency. The transport of hot electrons is currently modeled in *LSP* only from the end of the cone tip for cone-in-shell targets to the dense core, where the hot-electron energy is absorbed; the cone itself and the electron transport in the cone are not simulated.

The *LSP* part of the simulation starts when the high-energy, short-pulse laser is injected using the hydrodynamic profiles predicted by *DRACO*. *LSP* runs for a short time (~1 ps) during which the hydrodynamic evolution is minimal, and it generates a time history of hot-electron energy deposition. *DRACO* then runs for the same time, using the energy deposition calculated by *LSP* as an additional energy source in the temperature equation. The hydrodynamic profiles in *LSP* are updated according to the *DRACO* results, while the hot-electron distributions and the electromagnetic fields in *LSP* are left unchanged. *DRACO* and *LSP* are run together for the duration of the high-energy petawatt pulse. The hydrodynamic reaction of the target after the high-energy petawatt pulse is simulated by *DRACO*.

The first simulations of integrated fast-ignitor experiments planned for the combined OMEGA/OMEGA EP Laser System used 40-μm-thick CD shells of ~870-μm outer diameter, a gold cone with an opening angle of 35° and a tip thickness of 15 μm, irradiated by a highly shaped laser pulse of ~3-ns duration and ~20-kJ energy. Currently, radiation transport is not included in the hydro simulation, which leads to an overestimate of the compressed target density. The OMEGA EP laser is assumed to deliver 2.6 kJ in a 10-ps pulse into the cone, which is translated into a hot-electron distribution assuming a 30% conversion efficiency and a slope temperature according to the Wilks scaling. The hot electrons are given a Gaussian profile in the radial direction with a diameter of 20 μm (FWHM) and an angular spread of 20° (half-angle, FWHM). Figure 115.19 shows results

from these simulations as 2-D maps of (a) the plasma density, (b) hot-electron density, and (d) the azimuthal magnetic field in the r–z plane 6 ps after the beginning of the hot-electron pulse. Figure 115.19(c) shows the total plasma-temperature increase caused by the heating from hot electrons at the end of the laser pulse. The hot electrons are seen to be well collimated by the resistive magnetic field generated by the electron beam despite the high initial divergence. The maximum temperature increase in the core is of the order of 1 keV.

This *LSP*/*DRACO* code combination scheme was also used to perform integrated high-gain, fast-ignition simulations. An optimized spherically symmetric target imploded with a highly shaped 300-kJ compression pulse[7] was used, and the electron beam was injected 125 μm from the target center. The electron beam had a square profile in time with a duration of 10 ps and a Gaussian profile in the radial direction with a diameter of 30 μm (FWHM). A Maxwellian distribution was assumed for the electrons with a mean energy of 2 MeV and an angular spread of 20° (half-angle, FWHM). In contrast to the simulations of the experiments on OMEGA EP, these simulations show what is believed to be resistive filamentation, similar to observations in the hybrid simulations of Honrubia and Meyer-ter-Vehn.[59] For the given parameters, 43 kJ of energetic electrons were required for ignition, resulting in a gain of ~100. When the effect of the magnetic field on beam electrons was artificially suppressed, the minimum electron-beam energy required for ignition increased to 96 kJ, demonstrating the beneficial effect of the resistive magnetic field.

Summary

A comprehensive scientific program is being pursued at LLE to investigate the fast-ignitor concept for inertial confinement fusion. The combined OMEGA/OMEGA EP Laser Facility provides the experimental infrastructure for these investigations. The OMEGA EP laser was completed in April 2008. Two of the four OMEGA EP beamlines can operate in short-pulse mode, with up to 2.6 kJ each at a 10-ps pulse duration. These beams can be routed into either the OMEGA EP chamber or combined collinearly into the existing OMEGA target chamber for integrated fast-ignitor experiments. Fuel-assembly experiments on OMEGA with both room-temperature and cryogenic targets have achieved high fuel-areal densities of ~200 mg/cm^2, sufficient to stop the MeV electrons produced by the short-pulse laser. Experiments on the fuel assembly of cone-in-shell targets showed only a small deterioration of achievable areal density. The measured areal density was more than 60% of what a 1-D simulation predicts for an equivalent full sphere. The conversion efficiency from laser energy to fast electrons was measured using two independent experimental methods on both LLE's MTW laser and the RAL Vulcan Petawatt and found to be ~20% at intensities >10^{18} W/cm^2. A high-resolution (1.4-μm) TRD measures the coherent transition radiation from the rear side of a solid target, providing insight into the hot-electron transport. Simulation of both full-scale fast-ignition experiments and near-term integrated experiments on OMEGA, using a combination of a radiation hydrocode (*DRACO*) and a hybrid particle-in-cell code (*LSP*), shows the beneficial effects of the resistive magnetic fields generated by the propagation of the

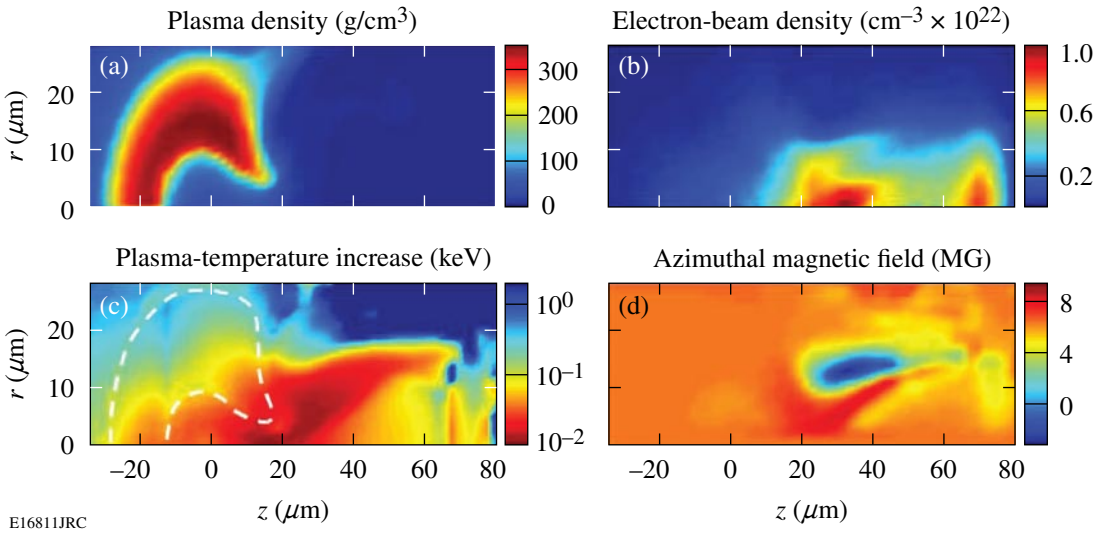

Figure 115.19
Snapshots of the (a) plasma density, (b) hot-electron density, and (d) the azimuthal magnetic field 6 ps after the beginning of the hot-electron pulse, for near-term, integrated fast-ignitor experiments on OMEGA. The maximum increase in plasma temperature (c) at the end of the pulse is ~1 keV

energetic electron into the high-density core. A decrease of the energy required to ignite a target imploded by a 300-kJ UV laser from ~100-kJ electron energy to ~40-kJ electron energy due to the magnetic fields was observed in simulations of full-scale fast-ignition targets. Simulations of fast-ignitor experiments with room-temperature cone-in-shell targets on OMEGA EP showed a temperature increase of up to 1 keV in the core with the short-pulse-laser–produced energetic electrons heating the target. Integrated experiments with room-temperature targets on the combined OMEGA/OMEGA EP Laser Facility are scheduled for the summer of 2008.

ACKNOWLEDGMENT

This work was supported by the U.S. Department of Energy Office of Inertial Confinement Fusion under Cooperative Agreement No. DE-FC52-08NA28302, Fusion Science Center, Office of Inertial Fusion Energy Science No. DE-FC02-ER54789, the University of Rochester, and the New York State Energy Research and Development Authority. The support of DOE does not constitute an endorsement by DOE of the views expressed in this article.

REFERENCES

1. N. G. Basov, S. Yu. Gus'kov, and L. P. Feokistov, J. Sov. Laser Res. **13**, 396 (1992).
2. M. Tabak *et al*., Phys. Plasmas **1**, 1626 (1994).
3. R. Kodama *et al*., Nature **412**, 798 (2001).
4. R. Kodama *et al*., Nature **418**, 933 (2002).
5. J. D. Lindl, R. L. McCrory, and E. M. Campbell, Phys. Today **45**, 32 (1992).
6. K. Yasuike *et al*., Rev. Sci. Instrum. **72**, 1236 (2001).
7. R. Betti, K. Anderson, J. Knauer, T. J. B. Collins, R. L. McCrory, P. W. McKenty, and S. Skupsky, Phys. Plasmas **12**, 042703 (2005).
8. J. Nuckolls *et al*., Nature **239**, 139 (1972).
9. C. K. Li and R. D. Petrasso, Phys. Rev. E **70**, 067401 (2004).
10. R. B. Stephens *et al*., Phys. Rev. E **69**, 066414 (2004).
11. Y. Kitagawa *et al*., Phys. Plasmas **9**, 2202 (2002).
12. P. A. Norreys *et al*., Phys. Plasmas **7**, 3721 (2000).
13. L. J. Waxer, D. N. Maywar, J. H. Kelly, T. J. Kessler, B. E. Kruschwitz, S. J. Loucks, R. L. McCrory, D. D. Meyerhofer, S. F. B. Morse, C. Stoeckl, and J. D. Zuegel, Opt. Photonics News **16**, 30 (2005).
14. T. R. Boehly, D. L. Brown, R. S. Craxton, R. L. Keck, J. P. Knauer, J. H. Kelly, T. J. Kessler, S. A. Kumpan, S. J. Loucks, S. A. Letzring, F. J. Marshall, R. L. McCrory, S. F. B. Morse, W. Seka, J. M. Soures, and C. P. Verdon, Opt. Commun. **133**, 495 (1997).
15. C. Stoeckl, C. Chiritescu, J. A. Delettrez, R. Epstein, V. Yu. Glebov, D. R. Harding, R. L. Keck, S. J. Loucks, L. D. Lund, R. L. McCrory, P. W. McKenty, F. J. Marshall, D. D. Meyerhofer, S. F. B. Morse, S. P. Regan, P. B. Radha, S. Roberts, T. C. Sangster, W. Seka, S. Skupsky, V. A. Smalyuk, C. Sorce, J. M. Soures, R. P. J. Town, J. A. Frenje, C. K. Li, R. D. Petrasso, F. H. Séguin, K. Fletcher, S. Padalino, C. Freeman, N. Izumi, R. Lerche, and T. W. Phillips, Phys. Plasmas **9**, 2195 (2002).
16. T. C. Sangster, R. Betti, R. S. Craxton, J. A. Delettrez, D. H. Edgell, L. M. Elasky, V. Yu. Glebov, V. N. Goncharov, D. R. Harding, D. Jacobs-Perkins, R. Janezic, R. L. Keck, J. P. Knauer, S. J. Loucks, L. D. Lund, F. J. Marshall, R. L. McCrory, P. W. McKenty, D. D. Meyerhofer, P. B. Radha, S. P. Regan, W. Seka, W. T. Shmayda, S. Skupsky, V. A. Smalyuk, J. M. Soures, C. Stoeckl, B. Yaakobi, J. A. Frenje, C. K. Li, R. D. Petrasso, F. H. Séguin, J. D. Moody, J. A. Atherton, B. D. MacGowan, J. D. Kilkenny, T. P. Bernat, and D. S. Montgomery, Phys. Plasmas **14**, 058101 (2007).
17. P. W. McKenty, V. N. Goncharov, R. P. J. Town, S. Skupsky, R. Betti, and R. L. McCrory, Phys. Plasmas **8**, 2315 (2001).
18. Y. Lin, T. J. Kessler, and G. N. Lawrence, Opt. Lett. **21**, 1703 (1996).
19. S. Skupsky and R. S. Craxton, Phys. Plasmas **6**, 2157 (1999).
20. T. R. Boehly, V. A. Smalyuk, D. D. Meyerhofer, J. P. Knauer, D. K. Bradley, R. S. Craxton, M. J. Guardalben, S. Skupsky, and T. J. Kessler, J. Appl. Phys. **85**, 3444 (1999).
21. G. H. Miller, E. I. Moses, and C. R. Wuest, Opt. Eng. **43**, 2841 (2004).
22. M. A. Rhodes *et al*., Appl. Opt. **34**, 5312 (1995).
23. B. W. Shore *et al*., J. Opt. Soc. Am. A **14**, 1124 (1997).
24. T. J. Kessler, J. Bunkenburg, H. Huang, A. Kozlov, and D. D. Meyerhofer, Opt. Lett. **29**, 635 (2004).
25. T. C. Sangster, V. N. Goncharov, P. B. Radha, V. A. Smalyuk, R. Betti, R. S. Craxton, J. A. Delettrez, D. H. Edgell, V. Yu. Glebov, D. R. Harding, D. Jacobs-Perkins, J. P. Knauer, F. J. Marshall, R. L. McCrory, P. W. McKenty, D. D. Meyerhofer, S. P. Regan, W. Seka, R. W. Short, S. Skupsky, J. M. Soures, C. Stoeckl, B. Yaakobi, D. Shvarts, J. A. Frenje, C. K. Li, R. D. Petrasso, and F. H. Séguin, Phys. Rev. Lett. **100**, 185006 (2008).
26. W. Theobald, R. Betti, C. Stoeckl, K. S. Anderson, J. A. Delettrez, V. Yu. Glebov, V. N. Goncharov, F. J. Marshall, D. N. Maywar, R. L. McCrory, D. D. Meyerhofer, P. B. Radha, T. C. Sangster, W. Seka, D. Shvarts, V. A. Smalyuk, A. A. Solodov, B. Yaakobi, C. D. Zhou, J. A. Frenje, C. K. Li, F. H. Séguin, R. D. Petrasso, and L. J. Perkins, Phys. Plasmas **15**, 056306 (2008).
27. V. N. Goncharov, T. C. Sangster, P. B. Radha, R. Betti, T. R. Boehly, T. J. B. Collins, R. S. Craxton, J. A. Delettrez, R. Epstein, V. Yu. Glebov, S. X. Hu, I. V. Igumenshchev, J. P. Knauer, S. J. Loucks, J. A. Marozas, F. J. Marshall, R. L. McCrory, P. W. McKenty, D. D. Meyerhofer, S. P. Regan, W. Seka, S. Skupsky, V. A. Smalyuk, J. M. Soures, C. Stoeckl, D. Shvarts, J. A. Frenje, R. D. Petrasso, C. K. Li, F. Séguin, W. Manheimer, and D. G. Colombant, Phys. Plasmas **15**, 056310 (2008).
28. V. N. Goncharov, J. P. Knauer, P. W. McKenty, P. B. Radha, T. C. Sangster, S. Skupsky, R. Betti, R. L. McCrory, and D. D. Meyerhofer, Phys. Plasmas **10**, 1906 (2003).

29. C. K. Li, D. G. Hicks, F. H. Séguin, J. A. Frenje, R. D. Petrasso, J. M. Soures, P. B. Radha, V. Yu. Glebov, C. Stoeckl, D. R. Harding, J. P. Knauer, R. L. Kremens, F. J. Marshall, D. D. Meyerhofer, S. Skupsky, S. Roberts, C. Sorce, T. C. Sangster, T. W. Phillips, M. D. Cable, and R. J. Leeper, Phys. Plasmas **7**, 2578 (2000).

30. J. Delettrez, R. Epstein, M. C. Richardson, P. A. Jaanimagi, and B. L. Henke, Phys. Rev. A **36**, 3926 (1987).

31. K. Anderson and R. Betti, Phys. Plasmas **11**, 5 (2004).

32. C. D. Zhou, W. Theobald, R. Betti, P. B. Radha, V. A. Smalyuk, D. Shvarts, V. Yu. Glebov, C. Stoeckl, K. S. Anderson, D. D. Meyerhofer, T. C. Sangster, C. K. Li, R. D. Petrasso, J. A. Frenje, and F. H. Séguin, Phys. Rev. Lett. **98**, 025004 (2007).

33. R. B. Stephens *et al*., Phys. Rev. Lett. **91**, 185001 (2003).

34. C. Stoeckl, T. R. Boehly, J. A. Delettrez, S. P. Hatchett, J. A. Frenje, V. Yu. Glebov, C. K. Li, J. E. Miller, R. D. Petrasso, F. H. Séguin, V. A. Smalyuk, R. B. Stephens, W. Theobald, B. Yaakobi, and T. C. Sangster, Phys. Plasmas **14**, 112702 (2007).

35. D. K. Bradley *et al*., Rev. Sci. Instrum. **66**, 716 (1995).

36. P. B. Radha, T. J. B. Collins, J. A. Delettrez, Y. Elbaz, R. Epstein, V. Yu. Glebov, V. N. Goncharov, R. L. Keck, J. P. Knauer, J. A. Marozas, F. J. Marshall, R. L. McCrory, P. W. McKenty, D. D. Meyerhofer, S. P. Regan, T. C. Sangster, W. Seka, D. Shvarts, S. Skupsky, Y. Srebro, and C. Stoeckl, Phys. Plasmas **12**, 056307 (2005).

37. J. A. Oertel *et al*., Rev. Sci. Instrum. **70**, 803 (1999).

38. P. K. Gupta *et al*., Appl. Phys. Lett. **39**, 32 (1981).

39. P. M. Nilson, W. Theobald, J. Myatt, C. Stoeckl, M. Storm, O. V. Gotchev, J. D. Zuegel, R. Betti, D. D. Meyerhofer, and T. C. Sangster, Phys. Plasmas **15**, 056308 (2008).

40. W. Theobald, K. Akli, R. Clarke, J. Delettrez, R. R. Freeman, S. Glenzer, J. Green, G. Gregori, R. Heathcote, N. Izumi, J. A. King, J. A. Koch, J. Kuba, K. Lancaster, A. J. MacKinnon, M. Key, C. Mileham, J. Myatt, D. Neely, P. A. Norreys, H.-S. Park, J. Pasley, P. Patel, S. P. Regan, H. Sawada, R. Shepherd, R. Snavely, R. B. Stephens, C. Stoeckl, M. Storm, B. Zhang, and T. C. Sangster, Phys. Plasmas **13**, 043102 (2006).

41. J. Myatt, W. Theobald, J. A. Delettrez, C. Stoeckl, M. Storm, T. C. Sangster, A. V. Maximov, and R. W. Short, Phys. Plasmas **14**, 056301 (2007).

42. C. N. Danson *et al*., Nucl. Fusion **44**, S239 (2004).

43. V. Bagnoud, I. A. Begishev, M. J. Guardalben, J. Puth, and J. D. Zuegel, Opt. Lett. **30**, 1843 (2005).

44. C. Stoeckl, W. Theobald, T. C. Sangster, M. H. Key, P. Patel, B. B. Zhang, R. Clarke, S. Karsch, and P. Norreys, Rev. Sci. Instrum. **75**, 3705 (2004).

45. Spectral Instruments, Tucson, AZ 85745.

46. S. C. Wilks *et al*., Phys. Rev. Lett. **69**, 1383 (1992).

47. A. J. Mackinnion *et al*., Phys. Rev. Lett. **88**, 215006 (2002).

48. Y. Sentoku *et al*., Phys. Rev. Lett. **90**, 155001 (2003).

49. H. Kolbenstvedt, J. Appl. Phys. **38**, 4785 (1967).

50. D. R. Welch *et al*., Nucl. Instrum. Methods Phys. Res. A **464**, 134 (2001).

51. Prism Computational Sciences, Inc., Madison, WI 53711.

52. S. D. Baton *et al*., Phys. Rev. Lett. **91**, 105001 (2003).

53. V. L. Ginzburg, Phys.-Usp. **39**, 973 (1996).

54. J. Zheng *et al*., Phys. Plasmas **10**, 2994 (2003).

55. W. L. Kruer, *The Physics of Laser Plasma Interactions*, Frontiers in Physics (Westview Press, Boulder, CO, 2003), pp. 39–43.

56. M. Storm, C. Guo, D. D. Meyerhofer, J. Myatt, T. C. Sangster, and C. Stoeckl, "Relativistic Electron-Beam Transport Measurements," to be published in Review of Scientific Instruments.

57. K. Miyamoto, *Plasma Physics for Nuclear Fusion*, Revised (MIT Press, Cambridge, MA, 1989).

58. L. Gremillet, G. Bonnaud, and F. Amiranoff, Phys. Plasmas **9**, 941 (2002).

59. J. J. Honrubia and J. Meyer-ter-Vehn, Nucl. Fusion **46**, L25 (2006).